TITLE: Understanding the mechanism of secondary cation release from the (001) surface of $Li(Ni_{1/3}Mn_{1/3}Co_{1/3})O_2$: insights from first principles

AUTHOR NAMES: Blake G. Hudson[a,‡], Diamond T. Jones [a,‡], Victoria M. Rivera Bustillo[a], Joseph W. Bennett[a], and Sara E. Mason [a,b,*]

AUTHOR ADDRESS:

[a]**Department of Chemistry,** University of Iowa, Iowa City, Iowa 52242, United States.

[b]**Center for Functional Nanomaterials, Brookhaven National Laboratory, Upton, New York 11973, United States**

[*]Corresponding Author: Sara E. Mason, Email: smason@bnl.gov ORCID 0000-0003-1515-6780

‡ These authors contributed equally to this work

KEYWORDS: metal release, density functional theory (DFT), surface transformations, machine learning

ABSTRACT

The transformations of complex metal oxides in aqueous settings must be studied to form a chemical understanding of how technologically relevant nanomaterials impact the environment upon disposal. Owing to the inherent heterogeneity and structural complexity of the ternary intercalation material $Li(Ni_xMn_yCo_{1-x-y})O_2$ (NMC), the mechanisms of chemical processes at the solid-water interface are challenging to model. Here, a density functional theory (DFT) + solvent ion methodology is used to study the energetics of subsequent release of two surface metals following unique pathways. The study spans different combinations of metal removal and also considers unique patterns of defects formed by modeling the NMC surface in supercells. The approach here also considers the equilibration of the surface with the surroundings between the successive metal removals. Machine learning is applied to rank the importance of different aspects of geometry and electronic structure in governing the energetic trends. A key finding is that a second metal removal prefers to proceed at the same site as the initial defect, and this is attributed in part to how the resulting slab with two metal vacancies maintains the most antiferromagnetic couplings between the remaining Ni/Mn.

Introduction

Lithium-ion batteries (LIBs) have substantially altered the landscape of technology and sustainable energy through their widespread applications in portable electronics, transportation, and energy storage[1, 2]. Despite its ubiquity, there are practical, if not also functional limitations of the prototypical cathode material, $LiCoO_2$ (LCO)[3]. The cost of LCO is driven upward due to low abundance of Co and its attributed mining costs[4-8]. Efforts to improve the efficiency at reduced cost use synthetic capabilities to replace Co sites in LCO with more abundant transition metals such as Ni and Mn[9]. The resulting materials have the general formula $Li(Ni_xMn_yCo_{1-x-y})O_2$ (NMC) and considerable research efforts have gone into tuning the metal ratios to optimize the cathode function[10-15]. NMC and other complex metal oxide cathode materials are in high demand with increases in production of portable electronics and electric vehicles. It is expected that 498 kilo tons on LIBs will be required in the year 2025, an increase of 243 kilo tons from 10 years prior[16]. Elemental abundance is a driver for materials design of cathode materials to reduce cost. To reclaim non-abundant metals such as Co and Li, recycling is not an easy solution as the required harsh chemical conditions add cost and a host of complications[17-22].

The confluence of increasing demand of complex metal oxides in electronics and limited recycling options leads to large amounts of these materials being disposed of[23-25]. It has been shown that landfill conditions enable the leaching of toxic metals from spent LIBs[26]. Furthermore, metal release from NMC materials has been identified as the route of toxicity to model organisms[27-32]. Metal release is a cross-cutting mechanism that can be advantageous and relevant beyond LIBs. This includes agricultural applications where the release of micro-nutrients (Cu, Zn, Ag, Ti, etc.) can help protect plants from disease, salinity, and improve germination[33-35]. Metal release is also important in regards to synthesis. Humidity conditions during the synthesis of NMC can cause metal dissolution leading to decreased functionality[36, 37]. Ultimately, a better understanding of how material properties and aqueous chemistry influence metal release is desirable as a means for guiding controlled release by design.

Using a DFT + solvent ion model methodology[38] adapted and corroborated in collaboration with experimental synthesis, characterization, analytical measurements, and biological studies, we have previously studied the NMC family of materials[39-41]. A prior experimental study of equistoichiometric NMC showed incongruent release of metals in water with the following trend, Ni > Co > Mn, as determined by ICP-MS measurements[27]. In the DFT + solvent ion model, electronic structure calculations for vacancy formation energies are used in combination with tabulated energetics for the formation of the preferred aqueous metal speciation. The model partitions the overall reaction into a vacancy formation step removing one metal and an -OH group as determined to be the most favorable pathway in previous work denoted as ΔG_1, and separate steps for the redox and/or hydration of the M, O, and H leaving group substituents with associated energies denoted as ΔG_2[42]. Furthermore, changes in reaction conditions away from standard state are taken into account through analytical correction terms. Finally, the terms are summed and reported as ΔG_{tot}, where negative values indicate favorable release of the M-OH group under the specified conditions. Further details of the model as applied to metal release are reported[39, 43]. When applied to equistoichiometric NMC, the DFT + solvent ion model captures the incongruent release trend computing negative values of ΔG_{tot}, Ni < Co < Mn.

Through DFT modeling and incorporation of experimental solvation energies, modeling takes into account the solid-state properties (at the quantum-mechanical level) and the aqueous chemistry. This allows trends to be interpreted through physiochemical properties. In

$Li_{1.00}$(NMC), charge neutrality dictates that the metals exist in the oxide as Ni^{2+}, Mn^{4+}, and Co^{3+}, while all of the metals prefer a hydrated 2+ speciation under a range of environmental pH values[44]. While there are many descriptors (aspects of geometry and electronic structure) that could dictate the trends in metal release, here the oxidation state of the transition metals can be interpreted as a key governing factor: The metal with the highest oxidation state in NMC is Mn and forms the strongest bonds with lattice oxygen hence releases from NMC the least. Upon release, Mn must undergo reduction from 4+ in the lattice 2+ in an aqueous environment. This motivated the idea to pursue NMC materials with enriched Mn content in hopes that the resulting stoichiometry would be more resistant to metal release. It was found, unexpectedly, that Mn release increases in Mn-rich NMC beyond what is attributed to changes in mole fraction. While Mn-rich NMC shows reduced amounts of Ni and Co release, which are the two toxic ions in solution, it is not sufficient to prevent the toxic impact towards model organisms.[27-29] Through the DFT + solvent ion model, the ΔG_{tot} values for Mn become more negative as the Mn mole fraction increases agreeing with experimental trends[40]. The electronic structure provides an interpretation: When increasing the relative amount of Mn in the lattice, Mn replaces some Ni^{2+} and Co^{3+} sites. Electronic structure analysis confirms that this gives rise to a composition that has a mixture of Mn^{4+}/Mn^{2+} in the lattice. Here the trend can be interpreted beyond the oxidation state argument by more closely considering the chemical environment: The d^3 Mn^{4+} is relatively more stable in the octahedral environment when compared to the high spin d^5 Mn^{2+}.

The interplay of oxidation state, electron configuration, and chemical environment can also be used to rationalize experimental release profiles for Ni-enriched compositions. A decrease in Ni release was observed for Ni-rich NMC[41, 45]. Electronic structure calculations showed the Ni-rich NMC had Ni existing in a range of 2+ to 4+ oxidation states. The d^8 Ni^{2+} is relatively unstable in the octahedral environment compared to d^6 $Ni^{4+}$and Ni^{4+} forms stronger bonds with oxygen than Ni^{2+}[41]. Controlling oxidation states by tuning metal composition is also key in controlling thermodynamic stability of oxygen[13]. In a study focused on LCO, DFT + solvent ion methodology was benchmarked using numerous DFT exchange-correlation functionals and in-plane surface supercell sizes[46]. The methodology has been extended to newly proposed formulations of the cathode, lithiation states, and nanomaterials used in agriculture [47-50].

The release of metal cations from the NMC family of materials in aqueous settings relates to the transition metal dissolution of electrode-active materials at solid-electrolyte interfaces see, for example[51-53]. We do not provide a comprehensive review of this complementary topic here but note common governing chemical principles such as the TM oxidation state and solubility. The dissolution of transition metal-bearing electrodes at the electrolyte interface can be correlated to cell performance degradation[54]. The current insufficient fundamental understanding of dissolution impedes material sciences approaches to improving the energy and power density of LIBs[55]. In particular, the dissolution of manganese has been studied at low potentials, where the discharged state of the cathode is coupled to manganese disproportionation and high potentials, where the manganese dissolution is thought to be linked to chemical delithiation by HF[56]. The interplay of metal dissolution and cycling performance has motivated efforts to use different electrolytes that are less sensitive to hydrolysis, to control HF production[57]. DFT has been used to track metal oxidation states associated with the state of charge to assist in understanding dissolution at the cathode electrode interface[51]. The flexible DFT + Thermodynamics framework used here for dissolution in aqueous settings could be explored to assist in developing molecular-level understanding of solid-electrolyte interfaces, particularly early stages of transition metal dissolution prior to the formation of the interphase.

All of the aforementioned DFT + solvent ion studies have only investigated a single metal release from the model slab. While important molecular-level understanding was derived from these studies, physical insights into the mechanism of metal release are limited in this approach, as is the ability to explain certain experimental observations. For example, it is reported that for NMC, dissolution leads to the formation of an Mn-rich phase, and an equilibrium where no further metal release is achieved[27, 29]. In this study we use the DFT + solvent ion model to investigate the stepwise removal of two *M*-OH groups (*M* = Ni, Mn, or Co) from the hydroxylated NMC surface, considering different pathways. In the present study, we focus on metal release as the early stage of dissolution[58]. The full dissolution process can go on to incur structural changes, which are known to occur at slower timescale not considered here.

Using the structural data obtained through multiple dissolution pathways, we assess three machine learning (ML) models to determine the best ML approach for ΔG_{tot} predictions and rank importance of features used to train the models. Results for the ML analysis are reported in the SI (S1) as we are unable to obtain substantial conclusions as the dataset is limited in size. We do report however that the importance of the features we relate to ΔG_{tot} agrees with our interpretations which suggests more meaningful insights could be obtained through a ML model in a study spanning a larger range of metal release values.

Theoretical Methods

Calculation Details

All DFT calculations in this study were performed using the Quantum ESPRESSO software package [59]. All calculations are spin polarized, with NMC modeled as ferrimagnetic, achieved by antiferromagnetic coupling between Ni and Mn as in previous work where this was found to be the most favorable configuration [39, 47]. Experimental studies on the magnetism of NMC have shown that between 100 and 300 K the magnetic ordering is paramagnetic[60]. This among other studies [61-63], also suggest there is random structural ordering of metals in the M-O layers. While it is challenging to experimentally characterize the details of cation ordering[64], the alternating pattern is consistent with Monte Carlo and Simulated-Annealing-based modeling for 333NMC[65]. Our calculations focus on the perfectly alternating configuration where each metal species is surrounded by two of each other metal, as shown in Figure 1. In this structural configuration, our DFT calculations show that antiferromagnetic ordering is favored with the spins of Ni aligned anti to those of Mn [66], and this ordering is used throughout. The PBE-GGA[67] exchange correlation functional was used, including Hubbard U correction values[68, 69], and the Kohn-Sham orbitals are expanded in a planewave basis set with a 40 Ry cutoff. All slab models are subject to geometry optimization, enforcing the inversion symmetry of the slab and under a convergence criteria of 5 meV/Å. Previous comparisons of optimized structures for hydroxylated oxide surfaces in the presence/absence of aqueous solvation effects show minimal impact on the O-H bond distances and the oxide inter-layer spacings, and all calculations here are done without use of continuum solvent models[70, 71]. The atoms in our calculations were represented using the GBRV ultrasoft pseudopotentials[72]. U-values of 6.40, 4.91, and 0.10 eV were used to obtain ideal oxidation states for Ni, Co, and Mn respectively. Based on previous testing of the effect of applying U corrections to Ni, Mn, and Co[39], we note that the calculated values of the Mn-OH removals showed discontinuous changes, even at moderate values of U. This, along with tracking the variation of the metal oxidation states as a function of U values (as detailed in S2. Table 1) guided the choice of U values in the study.

Surface calculations include at least 20 Å of vacuum between periodic repeats to prevent self-interaction between slabs. The surface models in this investigation were based on a $\sqrt{3}$ x $\sqrt{3}$ R30˚ rotated hexagonal unit cell of the delafossite structure type, with three metal sites. As shown later, this supercell supports nearest neighbor and next-nearest neighbor co-metal vacancies. To further separate the vacancies would require expansion to a computationally prohibitive supercell. From previous results (cite Ali paper) the metal release energies in the supercell used here will not to be independent of the supercell size but can be expected to vary linearly and thus be useful for examining trends. A 2 x 6 x 1 Monkhorst-Pack[73] k-point grid is used for all surface models. The $3\sqrt{3}$ x $\sqrt{3}$ supercell model has 9 total metal sites. Previous work measured metal dissolution for various morphologies of NMC including nanosheets, nano blocks, and commercial nanoparticles[28]. XRD measurements of the nanosheet identify the dominant facet as (001) and also measure the lowest surface free energy for this facet. The (001) facet is most found in cathodes and, additionally, findings show that when normalized by surface area, all morphologies have the same amount of metal release.

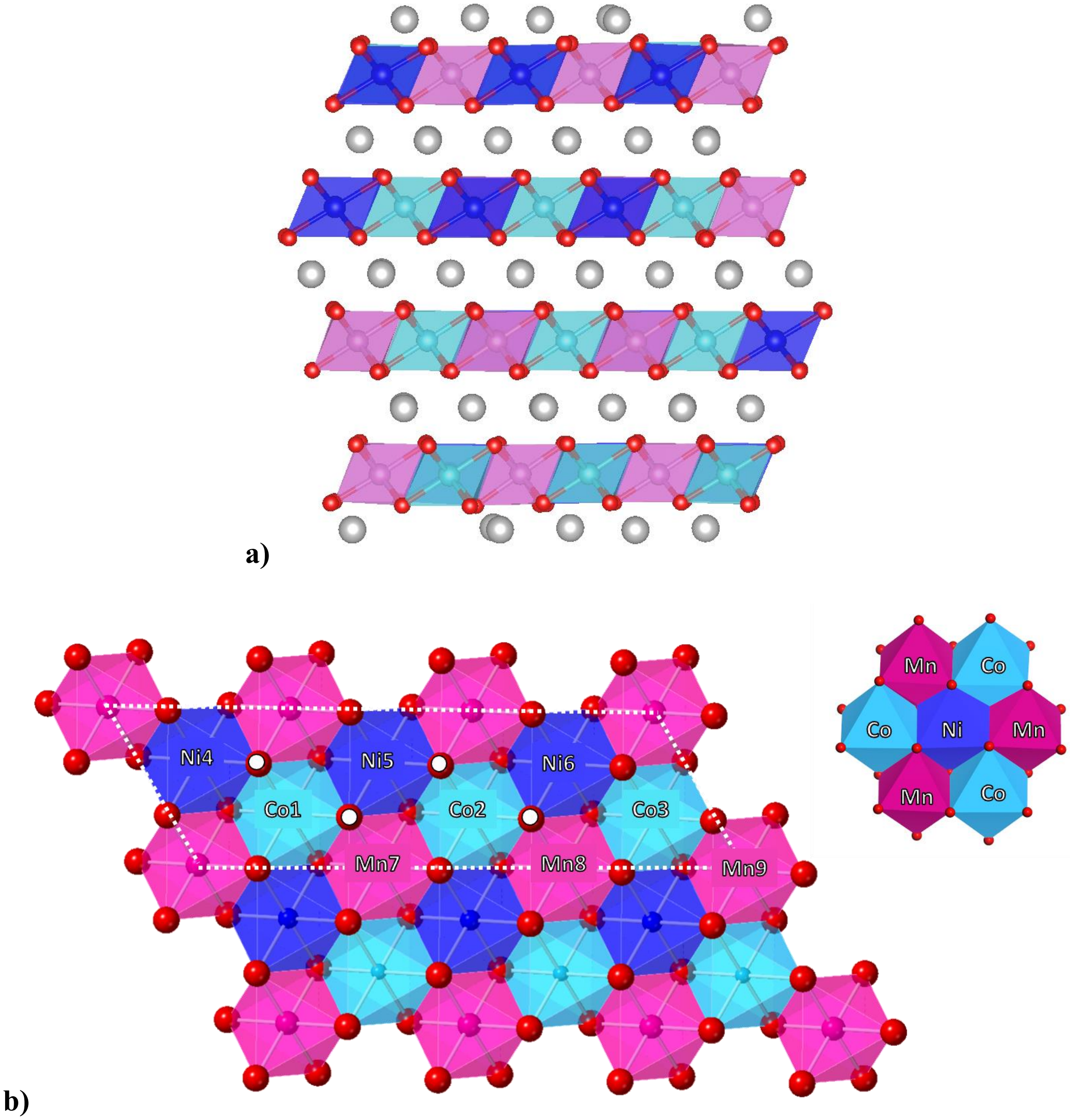

Figure 1: a) Side view of the ${}_{M'-OH}^{M-OH}NMC_{Li-term}$ slab, further detailed below in the methods. Ni is shown as dark blue, Co light blue, Mn magenta, O red, and Li grey. **b)** Defect free top-down view of the (001) (${}_{M'-OH}^{M-OH}NMC$) with surface layer metals labeled by elemental symbol and atom

number used to mark removal sites. The metals have the same color scheme and H is white. The $3\sqrt{3}x3$ supercell is denoted by the dashed white line. The top right shows a pictorial representation of the local environment for a Ni site.

The metals in the lattice are octahedrally coordinated to O in an edge-sharing configuration, and the Li is in channels between the oxygens of the O-*M*-O layers. Experimental characterization of these nanosheets have an average thickness of 2-15 Å[27]. Our model consists of four O-*M*-O layers, two inner layers to represent the bulk and two outer layers for the surface, related by inversion symmetry and resulting in a total slab thickness of ~18 Å. To model the NMC-water interface, the outermost Li atoms in the $3\sqrt{3}$ x $\sqrt{3}$ surface cell are replaced by H, which migrate from hollow sites to form hydroxyl groups with surface oxygen, as reported previously for LCO[71] and extrapolated to NMC[39]. Values of ΔE_1 are determined using DFT total energies are converted to Gibbs free energies by correcting for the zero-point energy and vibrational contributions, which for the slabs are approximated as coming from the surface -OH groups in the style of Rong and Kolpak[38] and confirmed sufficient for this structure type by Huang et al.[71].

Thermodynamic Method: DFT + Solvent Ion Model

Here, we incorporate aqueous effects into our model using the DFT + Solvent Ion method that has been used in previous works to model the energetics of metal release from metal oxide surfaces [38-41, 46, 50, 74]. The methodology is detailed here sufficiently to describe the elementary reaction steps. In doing so, we also define a nomenclature for the geometric models of surface slabs used to model the consecutive release of *M*-OH (*M* = Ni, Mn, or Co) groups from the NMC surface.

As in previous studies, our cycle begins with a Li/H exchange at the outermost layer of the slab, equation 1. Figure 1 (a) shows the Li terminated surface which has Li atoms directly over the metal sites. Upon substitution, H migrates directly over the O sites to generate -OH groups, Figure 1 (b). This step takes into account the (previously determined[71]) favorable transformation of the surface in going from UHV to ambient conditions. ${}^{M-\mathrm{OH}}_{M'-\mathrm{OH}}\mathrm{NMC}_{\mathrm{Li-term}}$ denotes the pristine starting slab terminated with Li. The prefixing sub/superscript *M*-OH labels are used to label the first and second *M*-OH groups removed in a stepwise fashion, where the superscript and subscript are the first and second metal removed, respectively. ${}^{M-\mathrm{OH}}_{M'-\mathrm{OH}}\mathrm{NMC}_{\mathrm{H-term}}$ denotes the defect-free starting slab that now has all outermost Li atoms replaced with H atoms. As described above, the H migrate to O atoms in the lattice to form -OH groups. Equation 1 represents the only step where the surface termination changes. The remaining steps describe the removal of *M*-OH groups, and we refer to the slab as ${}^{M-\mathrm{OH}}_{M'-\mathrm{OH}}\mathrm{NMC}$ for simplicity in later equations and discussion.

Equation 2 represents the removal of the first *M*-OH group from the ${}^{M-\mathrm{OH}}_{M'-\mathrm{OH}}\mathrm{NMC}$ surface to form a defect surface denoted ${}_{M'-\overline{\mathrm{OH}}}\mathrm{NMC}^{*}$, done on both sides of the symmetry-related surfaces in the supercell while maintaining inversion symmetry. Creating inversion symmetric vacancies cancels out dipoles removing the need for additional correction terms. Figure 1 depicts a top view of the ${}^{M-\mathrm{OH}}_{M'-\mathrm{OH}}\mathrm{NMC}$ slab, where each of the 9 metal sites is given a label based on the chemical symbol of the metal and a numerical value. The metal sites selected for the initial metal vacancy are Ni6, Mn8, and Co2 shown in Figure 1.

Electronically, the general reaction depicted in equation 2 is accompanied by the slab losing 2, 3, and 4 electrons for Ni, Co, and Mn *M*-OH leaving groups, respectively. Electronic structure analysis shows this is compensated for in the slab by oxidation of remaining transition metals[74]. However, one can also consider the defect surface ${}_{M'-\overline{\mathrm{OH}}}\mathrm{NMC}^{*}$ re-equilibrating with the surroundings and adsorbing H to cap the dangling oxygen bonds. To model this process, we form slabs starting from the ${}_{M'-\overline{\mathrm{OH}}}\mathrm{NMC}^{*}$ structures by adding H atoms to the oxygen atoms whose bonding environments are perturbed by the M-OH removal, as depicted generically in equation 3. We add enough H to the surface to electronically compensate for the M-OH species removed, specifically $x = 1, 2, 3$ for Ni, Co, and Mn, respectively, to form a new surface denoted as ${}_{M'-\overline{\mathrm{OH}}}\mathrm{NMC}$. We also calculated the secondary release cycle without this equilibration step and found that it is always the less energetically favorable pathway. This energetic comparison is shown in **S3. Tables 2-3**.

Eq 1. $${}^{M-\mathrm{OH}}_{M'-\mathrm{OH}}\mathrm{NMC}_{\mathrm{Li-term}} + 4\mathrm{H_2(g)} \rightarrow {}^{M-\mathrm{OH}}_{M'-\mathrm{OH}}\mathrm{NMC}_{\mathrm{H-term}} + 8\mathrm{Li(s)}$$

Eq 2. $${}^{M-\mathrm{OH}}_{M'-\mathrm{OH}}\mathrm{NMC} \rightarrow {}_{M'-\overline{\mathrm{OH}}}\mathrm{NMC}^{*} + 2M\mathrm{(s)} + \mathrm{O_2(g)} + \mathrm{H_2(g)}$$

Eq 3. $${}_{M'-\overline{\mathrm{OH}}}\mathrm{NMC}^{*} + x\,\mathrm{H_2(g)} \rightarrow {}_{M'-\overline{\mathrm{OH}}}\mathrm{NMC}$$

The most undercoordinated surface oxygens in ${}_{M'-\overline{\mathrm{OH}}}\mathrm{NMC}^{*}$ are determined through bond valance (BV) sums, equation 4. Ideally, the bond valance sum, V_i, should equal the absolute value of the oxidation state of the i$^{\mathrm{th}}$ atom using the specified fitting parameters R_a and B for a given oxidation state. Values of V_i are reported in valance units (v.u.). R_{ij} is the bond distance between atoms i, the atom of focus, and j, every other atom in the system. The R_a fitting parameter is obtained from Gagné *et al.*[75]. To obtain B for the metals, we set V_i equal to the ideal oxidation states for our transition metals, 2+, 3+, and 4+ for Ni, Co, and Mn, respectively and use the R_{ij} values from ${}^{M-\mathrm{OH}}_{M'-\mathrm{OH}}$NMC. In the case of equilibrating the surface, H is added to the O with the lowest BV sum.

Eq 4. $$V_i = \Sigma S_{ij} = \sum_j \exp\left(\frac{R_a - R_{ij}}{B}\right)$$

In the next step, the second group noted as M'-OH is removed from the slab to form the double vacancy surface, ${}^{\text{—}}_{\text{—}}$NMC, as shown in equation 5. Representations of the secondary vacancy pathways are shown in Schemes 1 and 2 below. Through combining chemical equations 1-3 & 5, we obtain equation 6 which represents the overall secondary removal process.

We can formulate an energy change associated with equation 6 by taking the sum of total energies for the products minus that of the reactants, weighted stoichiometrically and as shown in equation 7. Values of ΔE_1 determined using DFT total energies are converted to Gibbs free energies by correcting for the zero-point energy and vibrational contributions. Rong and Kolpak[38] and Huang et al.[71] approximate surface corrections of -OH groups are sufficient for this structure type.

Aqueous effects are added with additional elementary steps with associated energy changes denoted as ΔG_2, which is based on the Nernst equation and uses experimental ΔG°_{SHE} reference values[42]. This term is defined as: $\Delta G_2 = \Delta G^{\circ}_{SHE} - n_{e^-} eU_{SHE} - 2.3 * n_{H^+} * k_B T ln\left(a^{-Z}_{H_xAO_y}\right)$. $\Delta G^{\circ}_{\mathrm{SHE}}$ is the change in free energy to the aqueous species relative to the standard hydrogen electrode (SHE), U_{SHE} is the chemical potential relative to the SHE, n_{e^-} and n_{H^+} are the number of electrons and protons, respectively. The number of protons or electrons is metal-dependent. The concentration, *a*, is held constant at 1×10^{-6}, and $k_B T = (8.617 \times 10^{-5}$ eV/K) (298 K) = 0.0257 eV, and 2.3 is the conversion between *ln* and *log*. The SHE values that are used for each *M* depends on their oxidation states in aqueous media at a given pH and is determined using Pourbaix diagrams generated from Materials Project [44]. A table of ΔG_2 equations is provided in **S4.Table 4** and steps are shown going from equation 6 to equation 8 as this correction term is repeated for all standard state species. These corrective terms are added to our ΔG_1 equation to cancel out the standard state terms to arrive at ΔG_{tot}, equation 8. In this work, we present $\Delta G_{\mathrm{tot}} = \frac{\Delta G_1 + \Delta G_2}{2}$ to give the energy of release from one side of the slab. The number of electrons $(n)e^-$ on the right-hand side is dependent on both metals removed.

Eq 5. $${}^{\overline{\quad}}_{M'-\mathrm{OH}}\mathrm{NMC} \rightarrow {}^{\overline{\quad}}_{\underline{\quad}}\mathrm{NMC} + 2M'(\mathrm{s}) + \mathrm{O_2(g)} + \mathrm{H_2(g)}$$

Eq 6. $${}^{M-\mathrm{OH}}_{M'-\mathrm{OH}}\mathrm{NMC}_{\mathrm{Li-term}} + (2+x)\,\mathrm{H_2(g)} \rightarrow {}^{\overline{\quad}}_{\underline{\quad}}\mathrm{NMC} + 2M(\mathrm{s}) + 2M'(\mathrm{s}) + 2\mathrm{O_2(g)} + 8\mathrm{Li\ (s)}$$

Eq 7. $$\Delta E_1 = \left(E_{{}^{\overline{\quad}}_{\underline{\quad}}\mathrm{NMC}} + 2E_M + 2E_{M'} + 2E_{\mathrm{O_2}} + 8E_{\mathrm{Li}}\right) - \left(E_{{}^{M-\mathrm{OH}}_{M'-\mathrm{OH}}\mathrm{NMC}_{\mathrm{Li-term}}} + (2+\mathrm{x})\,E_{\mathrm{H_2}}\right)$$

Eq 8. $${}^{M-\mathrm{OH}}_{M'-\mathrm{OH}}\mathrm{NMC}_{\mathrm{Li-term}} + (2+x)\,\mathrm{H}^+_{(\mathrm{aq})} \rightarrow {}^{\overline{\quad}}_{\underline{\quad}}\mathrm{NMC} + M^{2+}_{(\mathrm{aq})} + M'^{2+}_{(\mathrm{aq})} + 2\,\mathrm{H_2O_{(l)}} + 4\mathrm{Li}^+_{(\mathrm{aq})} + (n)e^-$$

Structural Models for Secondary Metal Release

To model secondary release, we consider chemically unique sites for the removal of a second metal from ${}^{\overline{\quad}}_{M'-\mathrm{OH}}\mathrm{NMC}$. Our choice of the 3√3 x √3 NMC surface allows for 7 unique sites after initial vacancy formation, allowing us to examine release trends regarding the proximity to the initial vacancy. Larger supercells would be computationally taxing and reproduce the same release pathways. In a previous study investigating ΔG and supercell size[46], it was found that vacancy percentage has a linear trend with ΔG where it is easier to remove a metal from a larger surface. Ultimately, we chose the smallest cell to observe initial vacancy proximity dependence of ΔG as trends should scale with supercell size.

In **Scheme 1** we show the release of ${}^{\text{Ni-OH}}_{\text{Co}'\text{-OH (x)}}\text{NMC}$ to show the three unique Co sites after Ni removal. *x* denotes the 3 unique removal patterns which are displayed in the final step of Scheme 1. The first unique cobalt site is denoted as NN-I (nearest neighbor I) which is directly edge-sharing to the initial vacancy site. The second unique site is denoted as NN-II (nearest neighbor II) which is the other Co site that is edge sharing to the initial vacancy. This site differs from NN-I by creating a chain of vacancies with the repeat cells whereas NN-I has groupings of two vacancies that are separated by at least one metal. Lastly, we have our NNN (next nearest neighbor) removal which is the Co site that is not coordinated to the initial vacancy. Following Scheme 1

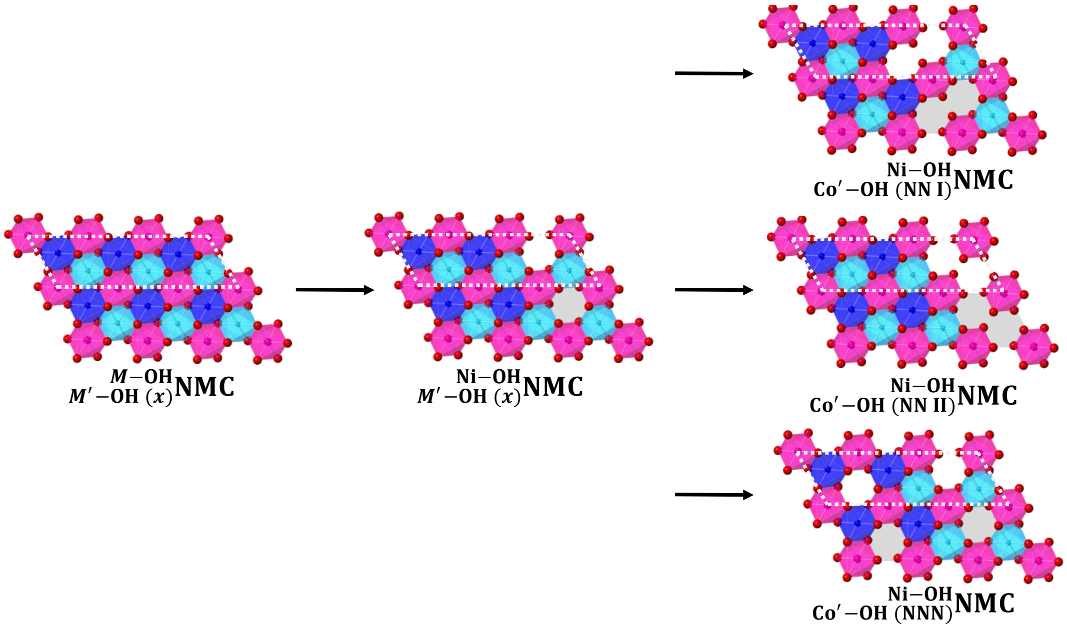

Scheme 1: Top-down polyhedral view of the initial Ni-OH and secondary removal of Co'-OH scheme. Ni is dark blue, Mn is magenta, Co is cyan, O is red, and the unit cell is outlined in a dashed white line. The unique site names, NN-I, NN-II and NNN, are listed below the picture where the periodic repeat vacancies are shaded in light grey.

as an example, the NN structures remove a Co that is edge sharing with the vacancy left by the initial Ni-OH removal. As shown through the periodic repeats in Scheme 1, NN-1 results in a double metal vacancy surrounded by occupied metal site. In comparison, the formation of NN-II creates a continuous row of defects in a zig-zag pattern across the surface. Finally, in the NNN structure, the vacancies do not share any oxygen atoms. When Mn is removed after the initial Ni vacancy, there are also these three unique sites which can be viewed in **S5.Figure 1** A distinct case is when two consecutive Ni-OH groups are removed. As shown in Scheme 2, there are two possible NNN structures labeled A and B.

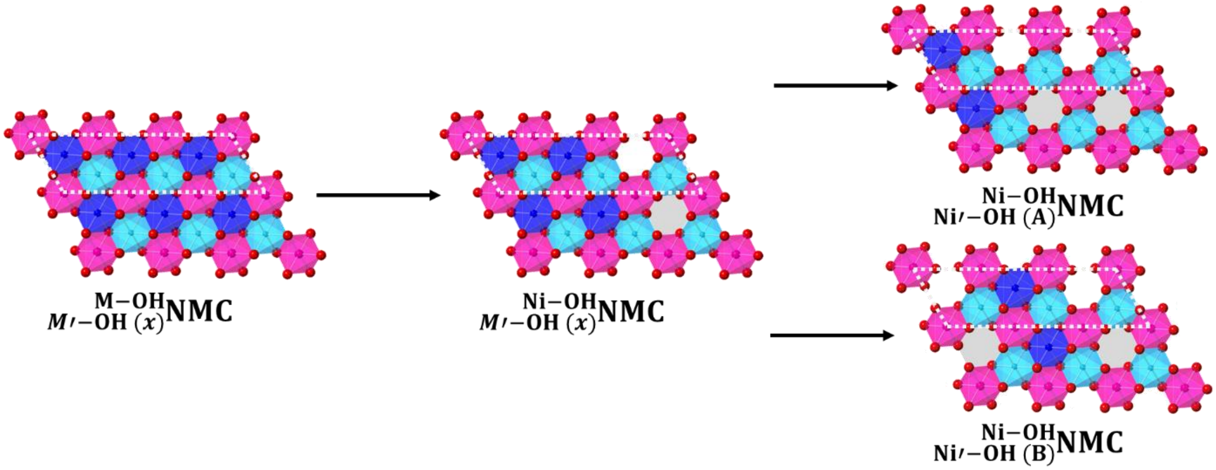

Scheme 2: The removal scheme for two Ni sites, A and B. Periodic repeats of vacancy sites are shaded in grey.

Results and Discussion

Equilibrating $_{M'-\overline{\text{OH}}}\text{NMC}^*$

Attempting to remove a second metal from the $_{M'-\overline{OH}}\text{NMC}^*$surface results in a very unfavorable ΔG_{tot}, values listed in **S3.Table 2**. After the initial vacancy, we observe oxidation of metals neighboring the vacancy site which can also be observed in the BV sums shown in Figure 2. The unfilled circles in Figure 2 represent the BV sums of the 8 remaining surface sites with Ni in blue, Mn in magenta, and Co in cyan. Many of the BV values of these metals are greater than the ideal oxidation state for ${}^{M-\mathrm{OH}}_{M'-\mathrm{OH}}\mathrm{NMC}$ resulting from the oxidized metals higher effective nuclear charge having a stronger bond towards oxygen. These stronger *M*-O bonds lead to unfavorable release values. We consider an additional step between metal release events where the surface is allowed to equilibrate with its surroundings as stated in equation 3 and find that this pathway is always more favorable for secondary release, as shown in **S3.Table 3**. As noted in the Methods section, values of V_i guide the choice of O sites for H addition to the least coordinated oxygens.

Comparing V_i values of the surface sites between ${}^{\overline{\phantom{-\mathrm{OH}}}}_{M'-\mathrm{OH}}\mathrm{NMC}^*$ and ${}^{\overline{\phantom{-\mathrm{OH}}}}_{M'-\mathrm{OH}}\mathrm{NMC}$ indicates the V_i values of the metals post equilibration are closer to ideal V_i values. There are two Co V_i values worth noting, ${}^{\mathrm{Ni-OH}}_{\mathrm{Co'-OH}\ (\mathrm{NN\ II})}\mathrm{NMC}$ and ${}^{\mathrm{Mn-OH}}_{\mathrm{Co'-OH}\ (\mathrm{NN\ II})}\mathrm{NMC}$, as their V_i values are lower than the other Co values in the given initial vacancy surface. These secondary removals are NN-II sites that are undercoordinated by one O from the initial vacancy, causing there to be fewer Co-O bonds in the summation of equation 4. Additionally, we observe Ni having V_i values less than 2 and Mn having V_i values greater than 4 due to the oxidation states of these metals. Post vacancy there are changes in bond lengths where the higher oxidation state metals shorten their bond distances with O causing the neighboring sites with lower oxidation states to have lengthened *M*-O distances. *M*-O distances surface atoms are provided in **S6.Tables 5-14**. This is observed in Figure 2 with Mn V_i values always overpredicted and Ni under.

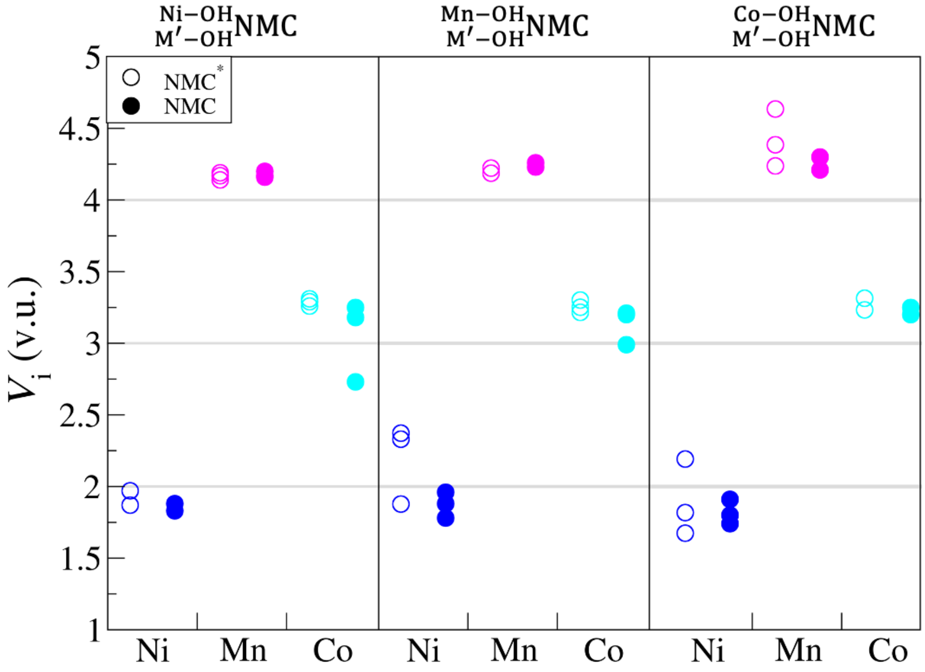

Figure 2: Bond valence sums of each metal site at the surface after initial vacancy formation with Ni shown in blue, Co, cyan, and Mn, pink. Empty circles represent BV sums before equilibration, and the filled circles post equilibration. Horizontal lines indicate nominal oxidation states of the transition metals in equistoichiometric NMC.

ΔG_{tot} Values

Computed values of ΔG_{tot} are provided in Table 1. When looking at the possible ways of removing Ni as the second metal, we observe 5 of 7 pathways yield favorable ΔG_{tot} values. When the identity of the second metal removed is Co, there are three pathways with negative ΔG_{tot} values, while in the case of Mn as the second metal removed there are no pathways predicted as favorable. Besides Ni having a greater number of favorable pathways to form doubly vacant ${}^{\_\_\_}_{\_\_\_}\text{NMC}$ slabs, the magnitude of ΔG_{tot} for Ni is noticeably larger than the other metals. Specifically, the average ΔG_{tot} values are -0.75, 0.29, and 1.97 eV for Ni, Co, and Mn, respectively. This initial observation is in-line our original findings that the release favorability follows the trend Ni > Co > Mn[39]. That is, the trend persists through the removal of a second *M'*-OH group. The fact that Mn-OH as a second removal is always unfavorable, and relatively less favorable compared to Ni-OH and Co-OH, provide corroboration and insight into the experimentally observed of Mn in the lattice after NMC is exposed to water after a long time (~72 hours[27]). A third dominant trend is that it is predominantly the case for pathways forming the $\_\__{(\overline{\text{NN}})}\text{NMC}$ slabs are more favorable than those that form the $\_\__{(\text{N}\overline{\text{NN}})}\text{NMC}$ surface. This means that it is more favorable to remove the second metal from an edge-sharing octahedral metal site as opposed to perturbing an in-tact octahedral surface unit.

Table 1: ΔG_{tot} values for secondary removal from each surface site at pH 7. The first column labels each row. When the secondary metal is the same identity of the initial metal removed, the average value is shown. All values are in eV.

Structure	${}^{\text{Ni-OH}}_{\text{Mn-OH}}\text{NMC}$	${}^{\text{Ni-OH}}_{\text{Co-OH}}\text{NMC}$	${}^{\text{Ni-OH}}_{\text{Ni-OH}}\text{NMC}$	${}^{\text{Mn-OH}}_{\text{Co-OH}}\text{NMC}$	${}^{\text{Mn-OH}}_{\text{Ni-OH}}\text{NMC}$	${}^{\text{Mn-OH}}_{\text{Mn-OH}}\text{NMC}$	${}^{\text{Co-OH}}_{\text{Ni-OH}}\text{NMC}$	${}^{\text{Co-OH}}_{\text{Mn-OH}}\text{NMC}$	${}^{\text{Co-OH}}_{\text{Co-OH}}\text{NMC}$
NN-I	1.72	-1.11	-1.90	1.03	0.32	1.65	-2.26	1.63	-1.04
NN-II	1.29	-1.14		1.92	-0.22		-1.36	3.44	
NNN	3.19	1.10		1.24	0.35		-0.20	0.90	

ΔG_{tot} Analysis

Values of descriptors and ΔG_{tot} are reported in Tables 2-4 below where the descriptor values presented are right before the removal of the *M*'-OH unit that results in ${}_{M'-\mathrm{OH}\,\overline{(\mathrm{x})}}\mathrm{NMC}$. Starting with Table 2, we analyze trends in ΔG_{tot} values after initially removing a Ni-OH.

Table 2: Values shown here are for secondary removals after an initial Ni-OH removal. The first column defines the surface structure, column 2 are the V_i values in v.u., column 3 is the *M*' site spin, column 3 is the sum of the neighboring spins, column 4 is the perturbation of the spin environment defined as $\Delta\rho_{\mathrm{s}} = |\sum\rho_{\mathrm{s}} - \rho_{\mathrm{s}}|$, and in the final column is the ΔG_{tot} in eV.

Structure	V_i	ρ_s	$\Sigma\rho_s$	$\Delta\rho_s$	ΔG_{tot}
${}^{\mathrm{Ni-OH}}_{\mathrm{Co'-OH}\,(\mathrm{NNN})}\mathrm{NMC}$	2.78	0.06	3.05	2.99	1.10
${}^{\mathrm{Ni-OH}}_{\mathrm{Co'-OH}\,(\mathrm{NN-I})}\mathrm{NMC}$	2.86	0.03	3.7	3.67	-1.11
${}^{\mathrm{Ni-OH}}_{\mathrm{Co'-OH}\,(\mathrm{NN-II})}\mathrm{NMC}$	2.39	0.75	5.75	5.00	-1.14
${}^{\mathrm{Ni-OH}}_{\mathrm{Ni'-OH}\,(\mathrm{B})}\mathrm{NMC}$	2.03	-1.70	8.89	10.59	-1.75
${}^{\mathrm{Ni-OH}}_{\mathrm{Ni'-OH}\,(\mathrm{A})}\mathrm{NMC}$	2.08	-1.70	7.79	9.49	-2.04
${}^{\mathrm{Ni-OH}}_{\mathrm{Mn'-OH}\,(\mathrm{NNN})}\mathrm{NMC}$	3.87	2.75	-4.95	7.70	3.19
${}^{\mathrm{Ni-OH}}_{\mathrm{Mn'-OH}\,(\mathrm{NN-II})}\mathrm{NMC}$	3.99	2.17	-0.89	3.06	1.29

${}^{\mathrm{Ni-OH}}_{\mathrm{Mn'-OH\,(NN-I)}}\mathrm{NMC}$	3.92	2.64	-1.84	4.48	1.72

For sites with an additional Ni removed, ${}^{\mathrm{Ni-OH}}_{\mathrm{Ni'-OH(x)}}\mathrm{NMC}$ (rows 4 & 5), we compare the trends in the spin. The A-site is more favorable by 0.29 eV with the largest associated descriptor change observed for $\Sigma\rho_s$ (which also causes the same change in $\Delta\rho_S$). Due to the change in $\Sigma\rho_s$, the spin environment after the Ni'-OH (A) site release generates a ${}^{\mathrm{Ni-OH}}_{\mathrm{Ni-OH\,(A)}}\mathrm{NMC}$ structure with fewer unpaired electrons than ${}^{\mathrm{Ni-OH}}_{\mathrm{Ni'-OH\,(B)}}\mathrm{NMC}$, thus forming the ${}^{\mathrm{Ni-OH}}_{\mathrm{Ni'-OH\,(A)}}\mathrm{NMC}$ is more favorable. In another instance, the formation of the ${}^{\mathrm{Ni-OH}}_{\mathrm{Mn'-OH\,(NN-II)}}\mathrm{NMC}$ surface (row 7) also shows a lower $\Delta\rho_s$ value and is associated with a more favorable ΔG_{tot} but goes on to show interesting dependence on the value of ρ_s. We observe that the ρ_s value decreases which suggests that this Mn' site is no longer Mn^{4+} with a d^3 configuration. This is shown in the projected density of states in Figure 3 with this Mn' site plotted in the middle. For analysis, the Fermi energy (E_F) is fixed at zero to show occupied orbitals below the Fermi line and unoccupied above. We observe some of the up-spin density moves above the fermi energy indicating this Mn' site has lost electron density in the t_{2g} orbitals showing this site has undergone oxidation. We would expect an oxidized metal to have a stronger bonding network to the surrounding oxygen atoms making it more difficult to remove this site. This interplay between metal-oxygen bond distances and metal oxidation state is explored quantitatively using a bond-valence analysis and as presented in S6.Table 15. However, the removal of two neighboring Ni sites causes $\Sigma\rho_s$ to decrease showing that $\Delta\rho_s$ can outweigh the oxidation state trends we have seen for our studies only looking at a single *M*-OH removal.[39-41, 47].

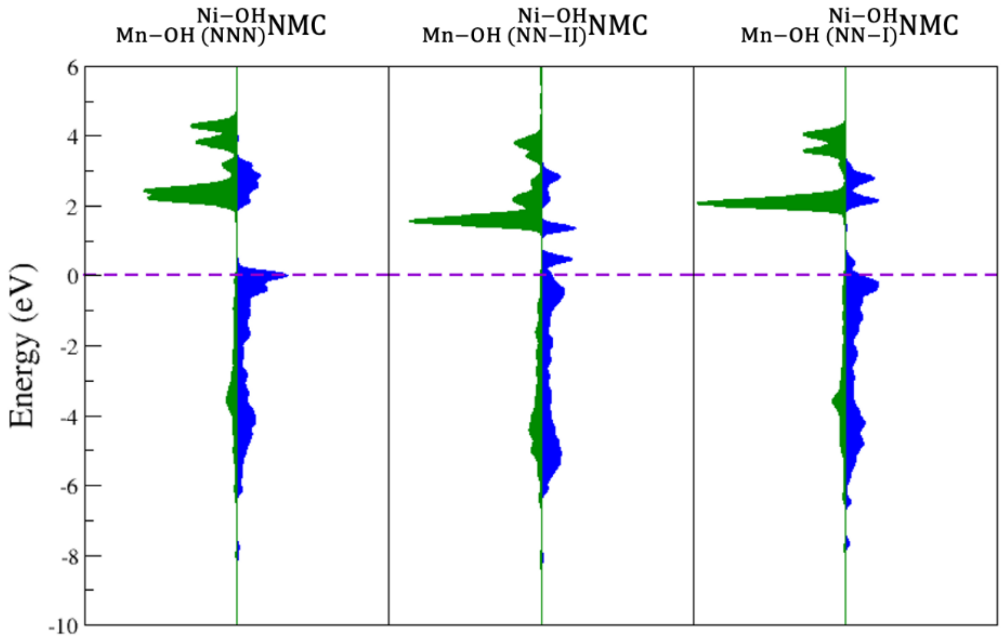

Figure 3: Projected density of states of Mn' after initial Ni removal. The spin up density is shown as blue, and the spin down density of shown in green. The Fermi energy (E_F) is denoted with the dashed purple line. The projected densities presented in this work fix E_F at zero by subtracting E_F over all energy levels (E-E_F).

The (001) surface prefers to maintain an AFM spin alignment, and this controls metal release trends, as the remaining metals undergo redox to maintain this spin alignment. This leads to the main takeaway that: When there is a $\Delta\rho_s$ value close to zero in a given $_{M'-\mathrm{OH}}\,^{\overline{\quad}}$NMC surface, the release of M'-OH will proceed more favorably to form a specific $\underline{\overline{\quad}}$NMC surface with a lower number of unpaired spins. The trend that most favorable M'-OH removals result in $\underline{\overline{\quad}}$NMC surfaces with a lower number of unpaired spins is violated by a few pathways that form a $_{\underline{\quad}\,(\mathrm{NN-I})}^{\overline{\quad}}$NMC surface. These exceptions can be explained by looking at V_i and ρ_s values. Table 2 shows that the formation of $_{\mathrm{Co'-OH}}\,^{\mathrm{Ni-OH}}_{(\mathrm{NN-II})}$NMC is the most favorable Co'-OH leaving group even though it has the largest $\Delta\rho_s$ value. This site has a V_i value that is about 0.4 v.u. less than the other Co sites and a ρ_s value of 0.75 indicating that this site has undergone a redox event and has an up-spin electron that is aligned in the same direction as the edge-sharing metals. By having an electron in the same direction as the surrounding metals we expect there to be a repulsive effect that destabilizes this site causing ${}_{\mathrm{Co'-OH}}{}^{\mathrm{Ni-OH}}_{\mathrm{(NN-II)}}\mathrm{NMC}$ (row 3) to be more favorable to form.

${}_{\mathrm{Co'-OH}}{}^{\mathrm{Mn-OH}}_{\mathrm{(NN-II)}}\mathrm{NMC}$ (Table 3, row 2) shows a decrease in the V_i value while there is not a large change in the associated ρ_s value. The V_i value has decreased due to having two vacancies in the neighboring environment and do not observe any changes in the electronic structure of Co2 (Figure 4).

Table 3: Values shown here are for secondary removals after an initial Mn-OH removal. The first column defines the surface structure, column 2 are the V_i values in v.u., column 3 is the *M*' site spin, column 3 is the sum of the neighboring spins, column 4 is the perturbation of the spin environment defined as $\Delta\rho_s = |\sum\rho_s - \rho_s|$, and in the final column is the ΔG_{tot} in eV.

Structure	V_i	ρ_s	$\Sigma\rho_s$	$\Delta\rho_s$	ΔG_{tot}
${}_{Co'-OH\,(NNN)}^{Mn-OH}NMC$	2.81	0.06	3.21	3.15	1.24
${}_{Co'-OH\,(NN-II)}^{Mn-OH}NMC$	2.68	0.13	-2.23	2.36	1.92
${}_{Co'-OH\,(NN-I)}^{Mn-OH}NMC$	2.82	0.03	0.39	0.35	1.03
${}_{Ni'-OH\,(NNN)}^{Mn-OH}NMC$	2.16	-1.68	8.32	10	0.35
${}_{Ni'-OH\,(NN-I)}^{Mn-OH}NMC$	1.97	-1.67	5.87	7.54	0.32
${}_{Ni'-OH\,(NN-II)}^{Mn-OH}NMC$	2.08	-1.66	2.89	4.55	-0.22
${}_{Mn'-OH\,(A)}^{Mn-OH}NMC$	3.94	2.77	-4.78	7.55	2.37
${}_{Mn'-OH\,(B)}^{Mn-OH}NMC$	3.97	2.7	-4.9	7.6	0.92

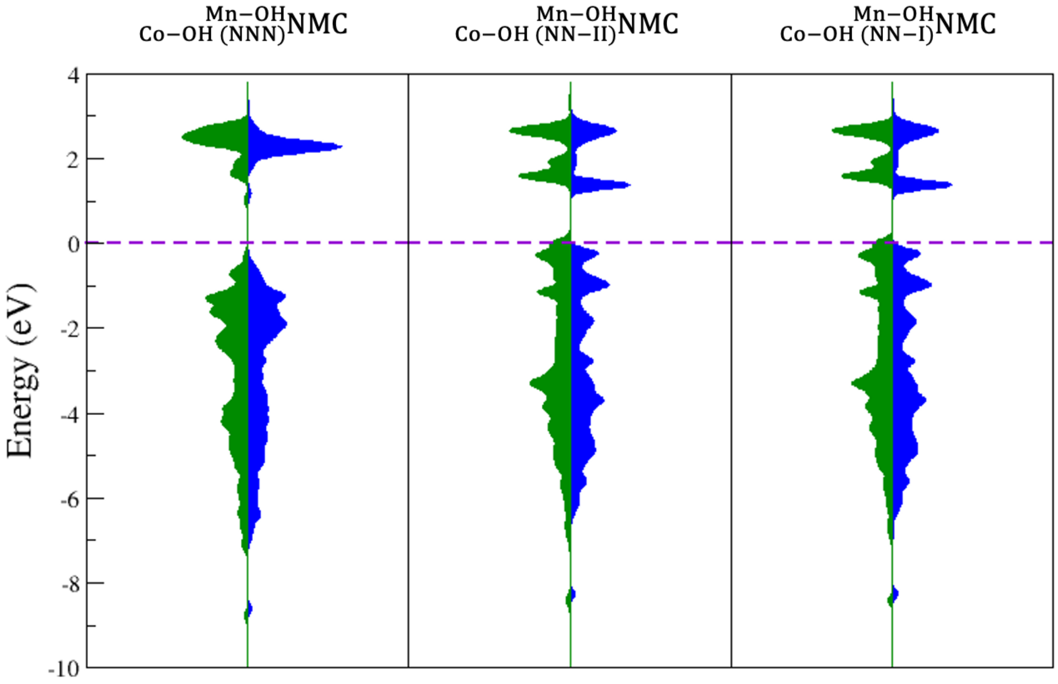

Figure 4: Projected density of states for Co’ after initial Mn removal. The color scheme is the same as Figure 3.

If we compare the Co-O bond distances of these three sites (**S6.Table 11**), we observe that the bonding strength of Co2 has increased to compensate for the two nearby vacancies, indicated by the shortening of the Co-O bonds.

${}^{\text{Co−OH}}_{\text{Mn}'\text{−OH (NN−II)}}\text{NMC}$ (Table 4, row 7) is very unfavorable to remove as well. Here we observe an increase in the V_i value and a decrease in ρ_s. The electronic structure for the Mn’-OH sites are shown in Figure 5 showing a change in the fillings for Mn8 that indicates the oxidation of Mn with some of the up-spin density moving above the fermi energy.

Table 4: Values shown here are for secondary removals after an initial Co-OH removal. The first column defines the surface structure, column 2 are the V_i values in v.u., column 3 is the *M*' site spin, column 3 is the sum of the neighboring spins, column 4 is the perturbation of the spin environment defined as $\Delta\rho_{\mathrm{s}} = |\sum\rho_{\mathrm{s}} - \rho_{\mathrm{s}}|$, and in the final column is the ΔG_{tot} in eV.

Structure	V_i	ρ_s	$\Sigma\rho_s$	$\Delta\rho_s$	ΔG_{tot}
${}^{Co-OH}_{Co'-OH\,(A)}NMC$	2.83	0.05	3.06	3.01	-0.93
${}^{Co-OH}_{Co'-OH\,(B)}NMC$	2.86	0.04	2.6	2.56	-1.14
${}^{Co-OH}_{Ni'-OH\,(NNN)}NMC$	2.12	-1.71	8.32	10.03	-0.2
${}^{Co-OH}_{Ni'-OH\,(NN-II)}NMC$	1.92	-1.71	7.62	9.33	-1.36
${}^{Co-OH}_{Ni'-OH\,(NN-I)}NMC$	1.99	-1.68	7.13	8.81	-2.26
${}^{Co-OH}_{Mn'-OH\,(NN-I)}NMC$	3.93	2.71	-5.03	7.75	1.63
${}^{Co-OH}_{Mn'-OH\,(NN-II)}NMC$	4.16	2.14	-5.03	7.17	3.08
${}^{Co-OH}_{Mn'-OH\,(NNN)}NMC$	3.92	2.76	-4.96	7.72	0.9

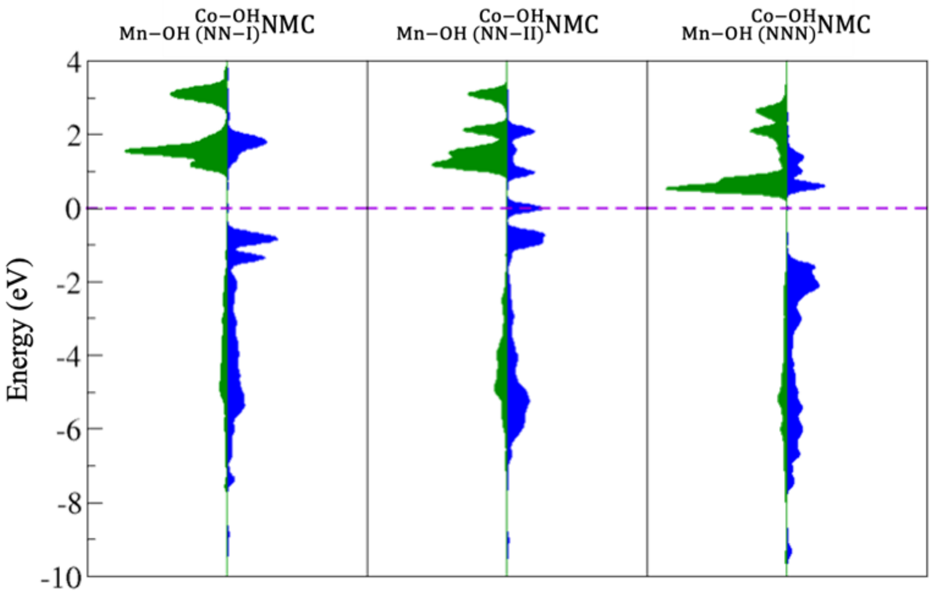

Figure 5: Projected density of states for Mn’ after initial Co removal. The color scheme is the same as Figure 3.

The oxidation of this site causes Mn8 to have a stronger bonding network with its surroundings which results in an increase in V_i above the ideal value of 4, even though there are two vacancies surrounding this site which we would have expected to lower V_i. The oxidation of this site gives us the least favorable Mn’-OH removal in Table 4.

As noted above, formation of $\underline{—}$NMC surfaces in NN patterns are generally more favorable than NNN patterns, but there are preferences for NN-I vs NN-II depending on the initial removal. After an initial removal of Ni-OH, forming the $_{\text{Co}'-\text{OH}}{}^{\text{Ni}-\text{OH}}_{(\text{NN}-\text{II})}\text{NMC}$ (Table 2, row 3) surface is most favored while after an initial Co-OH removal it is most favored to form the $_{\text{Ni}'-\text{OH}}{}^{\text{Co}-\text{OH}}_{(\text{NN}-\text{I})}\text{NMC}$ surface (Table 4, row 1). We predict that the removal of Co does not dramatically affect $\Sigma\rho_s$ since Co is in a d^6 configuration with no spin. Removing two of these sites around a Ni atom does not induce any changes in $\Sigma\rho_s$ but does cause Ni to form stronger bonds to O neighbors. Thus, Ni removal will follow pathways to form ${}_{\mathrm{Ni'-OH}}{}^{\mathrm{Co-OH}}_{\mathrm{(NN-I)}}\mathrm{NMC}$ over ${}_{\mathrm{Ni'-OH}}{}^{\mathrm{Co-OH}}_{\mathrm{(NN-II)}}\mathrm{NMC}$ (Table 4, row 4). When Ni is removed, there is a disturbance in $\Sigma\rho_s$ which causes ${}_{\mathrm{Ni'-OH}}{}^{\mathrm{Co-OH}}_{\mathrm{(NN-II)}}\mathrm{NMC}$ to become more favorable to form since Ni was providing anti-ferromagnetic coupling with neighboring Mn.

Conclusions

Different stepwise pathways to form NMC slabs with a total of two missing metal sites were modeled using a DFT + solvent ion methodology that enables electronic structure analysis of the solid state with the inclusion of aqueous effects provided by experimental data. The overall trend of incongruent release, with relative favorability of metal removal ranked as Ni > Co > Mn is maintained in going from surfaces with one to two metal vacancies. New mechanistic insights point to the preference for NMC to further dissolve through metal sites that are edge-sharing with an initial metal vacancy, as opposed to forming multiple isolated defect sites. The DFT + solvent ion model predicts the more favorable pathways to double vacancy formation have structures that help maintain a low net spin and favorable spin couplings. The stepwise modeling shows that when Mn is the identity of the second metal removed, the associated energetics are never favorable. This is in-line with experimental observations that over long periods of time, NMC in water forms a Mn-rich phase. While obvious descriptors such as oxidation sate play a governing role in the model energetics, RFT testing R^2 values are too low to be conclusive. Descriptor importance tracks with our interpretation that oxidative factors outweigh those related to spin coupling as spin is used more so to distinguish metal release trends after separating bins based on metal identity. Future directions regarding machine learned

ΔG_{tot} predictions could be targeted towards a more expansive range of structures with varying metal ratios and identities to create a model that can tailor release properties based on the composition. Furthermore, the methods outlined in this paper could be utilized as the basis for an expanded model to more complex metal release mechanisms that include ions and organic molecules that are commonly found aqueous media or metal release within the functioning environment of LIBs that incorporate electrolyte and anode.

Funding Sources

This work was supported by National Science Foundation under the NSF Center for Sustainable Nanotechnology, CHE-2001611.

Acknowledgements

This work is supported by the National Science Foundation under Grant No. CHE-2001611, the NSF Center for Sustainable Nanotechnology (CSN). This research used the Theory and Computation facility of the Center for Functional Nanomaterials (CFN), which is a U.S. Department of Energy **Office of Science User Facility**, at Brookhaven National Laboratory under Contract No. DE-SC0012704. We thank the support of the UI CLAS B&S fellowship and UI HPC computing resources used in this work. The work used the Extreme Science and Engineering Discovery Environment (XSEDE).

References

1. Yoshino, A., The Birth of the Lithium-Ion Battery. *Angewandte Chemie International Edition* **2012,** *51* (24), 5798-5800.
2. Goodenough, J. B.; Park, K.-S., The Li-Ion Rechargeable Battery: A Perspective. *Journal of the American Chemical Society* **2013,** *135* (4), 1167-1176.
3. Mizushima, K.; Jones, P. C.; Wiseman, P. J.; Goodenough, J. B., LixCoO2 (0<x<-1): A new cathode material for batteries of high energy density. *Materials Research Bulletin* **1980,** *15* (6), 783-789.
4. Sun, Y.-K.; Myung, S.-T.; Park, B.-C.; Prakash, J.; Belharouak, I.; Amine, K., High-energy cathode material for long-life and safe lithium batteries. *Nature Materials* **2009,** *8* (4), 320-324.
5. Poizot, P.; Laruelle, S.; Grugeon, S.; Dupont, L.; Tarascon, J. M., Nano-sized transition-metal oxides as negative-electrode materials for lithium-ion batteries. *Nature* **2000,** *407* (6803), 496-9.
6. Kang, D. H.; Chen, M.; Ogunseitan, O. A., Potential environmental and human health impacts of rechargeable lithium batteries in electronic waste. *Environ Sci Technol* **2013,** *47* (10), 5495-503.
7. Kang, K.; Meng, Y. S.; Bréger, J.; Grey, C. P.; Ceder, G., Electrodes with high power and high capacity for rechargeable lithium batteries. *Science* **2006,** *311* (5763), 977-80.
8. Farjana, S. H.; Huda, N.; Parvez Mahmud, M. A.; Saidur, R., A review on the impact of mining and mineral processing industries through life cycle assessment. *Journal of Cleaner Production* **2019,** *231*, 1200-1217.
9. Ceder, G.; Chiang, Y. M.; Sadoway, D. R.; Aydinol, M. K.; Jang, Y. I.; Huang, B., Identification of cathode materials for lithium batteries guided by first-principles calculations. *Nature* **1998,** *392* (6677), 694-696.
10. Ohzuku, T.; Makimura, Y., Layered Lithium Insertion Material of LiNi1/2Mn1/2O2 : A Possible Alternative to LiCoO2 for Advanced Lithium-Ion Batteries. *Chemistry Letters* **2001,** *30* (8), 744-745.
11. Chakraborty, A.; Kunnikuruvan, S.; Kumar, S.; Markovsky, B.; Aurbach, D.; Dixit, M.; Major, D. T., Layered Cathode Materials for Lithium-Ion Batteries: Review of Computational Studies on LiNi1–x–yCoxMnyO2 and LiNi1–x–yCoxAlyO2. *Chemistry of Materials* **2020,** *32* (3), 915-952.
12. Susai, F. A.; Sclar, H.; Shilina, Y.; Penki, T. R.; Raman, R.; Maddukuri, S.; Maiti, S.; Halalay, I. C.; Luski, S.; Markovsky, B.; Aurbach, D., Horizons for Li-Ion Batteries Relevant to Electro-Mobility: High-Specific-Energy Cathodes and Chemically Active Separators. *Advanced Materials* **2018,** *30* (41), 1801348.
13. Zheng, J.; Liu, T.; Hu, Z.; Wei, Y.; Song, X.; Ren, Y.; Wang, W.; Rao, M.; Lin, Y.; Chen, Z.; *et al.* Tuning of Thermal Stability in Layered Li(NixMnyCoz)O2. *Journal of the American Chemical Society* **2016,** *138* (40), 13326-13334.
14. Shao, Q.; Gao, P.; Yan, C.; Gao, M.; Du, W.; Chen, J.; Yang, Y.; Gan, J.; Wu, Z.; Zhang, C.-Y.; *et al.* A Redox Couple Strategy Enables Long-Cycling Li- and Mn-Rich Layered Oxide Cathodes by Suppressing Oxygen Release. *Advanced Materials* **2022,** *34*.
15. Hu, E.; Yu, X.; Lin, R.; Bi, X.; Lu, J.; Bak, S. M.; Nam, K. W.; Xin, H. L.; *Jaye, C.; Fischer, D. A.; et al.* Evolution of redox couples in Li- and Mn-rich cathode materials and mitigation of voltage fade by reducing oxygen release. *Nature Energy* **2018,** *3*, 690-698.

16. Choubey, P. K.; Chung, K.-S.; Kim, M.-s.; Lee, J.-c.; Srivastava, R. R., Advance review on the exploitation of the prominent energy-storage element Lithium. Part II: From sea water and spent lithium ion batteries (LIBs). *Minerals Engineering* **2017,** *110*, 104-121.
17. Tran, M. K.; Rodrigues, M.-T. F.; Kato, K.; Babu, G.; Ajayan, P. M., Deep eutectic solvents for cathode recycling of Li-ion batteries. *Nature Energy* **2019,** *4* (4), 339-345.
18. Chen, X.; Chen, Y.; Zhou, T.; Liu, D.; Hu, H.; Fan, S., Hydrometallurgical recovery of metal values from sulfuric acid leaching liquor of spent lithium-ion batteries. *Waste Management* **2015,** *38*, 349-356.
19. Bernardes, A. M.; Espinosa, D. C. R.; Tenório, J. A. S., Recycling of batteries: a review of current processes and technologies. *Journal of Power Sources* **2004,** *130* (1), 291-298.
20. Choi, J.-W.; Kim, J.; Kim, S.-K.; Yun, Y.-S., Simple, green organic acid-based hydrometallurgy for waste-to-energy storage devices: Recovery of NiMnCoC2O4 as an electrode material for pseudocapacitor from spent LiNiMnCoO2 batteries. *Journal of Hazardous Materials* **2022,** *424*, 127481.
21. Wu, J.; Zheng, M.; Liu, T.; Wang, Y.; Liu, Y.; Nai, J.; Zhang, L.; Zhang, S.; Tao, X., Direct recovery: A sustainable recycling technology for spent lithium-ion battery. *Energy Storage Materials* **2023,** *54*, 120-134.
22. Pinegar, H.; Smith, Y. R., Recycling of End-of-Life Lithium Ion Batteries, Part I: Commercial Processes. *Journal of Sustainable Metallurgy* **2019,** *5* (3), 402-416.
23. Kumar, J.; Neiber, R. R.; Park, J.; Ali Soomro, R.; Greene, G. W.; Ali Mazari, S.; Young Seo, H.; Hong Lee, J.; Shon, M.; Wook Chang, D.; Yong Cho, K., Recent progress in sustainable recycling of LiFePO4-type lithium-ion batteries: Strategies for highly selective lithium recovery. *Chemical Engineering Journal* **2022,** *431*, 133993.
24. Zhu, H.; Bai, Y.; Zu, L.; Bi, H.; Wen, J. Separation of Metal and Cathode Materials from Waste Lithium Iron Phosphate Battery by Electrostatic Process *Separations* [Online], 2023.
25. Wang, Y.; Tang, B.; Shen, M.; Wu, Y.; Qu, S.; Hu, Y.; Feng, Y., Environmental impact assessment of second life and recycling for LiFePO4 power batteries in China. *Journal of Environmental Management* **2022,** *314*, 115083.
26. Kang, D. H. P.; Chen, M.; Ogunseitan, O. A., Potential Environmental and Human Health Impacts of Rechargeable Lithium Batteries in Electronic Waste. *Environmental Science & Technology* **2013,** *47* (10), 5495-5503.
27. Hang, M. N.; Gunsolus, I. L.; Wayland, H.; Melby, E. S.; Mensch, A. C.; Hurley, K. R.; Pedersen, J. A.; Haynes, C. L.; Hamers, R. J., Impact of Nanoscale Lithium Nickel Manganese Cobalt Oxide (NMC) on the Bacterium Shewanella oneidensis MR-1. *Chemistry of Materials* **2016,** *28* (4), 1092-1100.
28. Hang, M. N.; Hudson-Smith, N. V.; Clement, P. L.; Zhang, Y.; Wang, C.; Haynes, C. L.; Hamers, R. J., Influence of Nanoparticle Morphology on Ion Release and Biological Impact of Nickel Manganese Cobalt Oxide (NMC) Complex Oxide Nanomaterials. *ACS Applied Nano Materials* **2018,** *1* (4), 1721-1730.
29. Gunsolus, I. L.; Hang, M. N.; Hudson-Smith, N. V.; Buchman, J. T.; Bennett, J. W.; Conroy, D.; Mason, S. E.; Hamers, R. J.; Haynes, C. L., Influence of nickel manganese cobalt oxide nanoparticle composition on toxicity toward Shewanella oneidensis MR-1: redesigning for reduced biological impact. *Environmental Science: Nano* **2017,** *4* (3), 636-646.
30. Marín Rodríguez, B.; Coppola, F.; Conradi, M.; Freitas, R., The impact of temperature on lithium toxicity in the gastropod Tritia neritea. *Environmental Science and Pollution Research* **2022,** *29*, 64745 - 64755.

31. Niemuth, N. J.; Curtis, B. J.; Hang, M. N.; Gallagher, M. J.; Fairbrother, D. H.; Hamers, R. J.; Klaper, R. D., Next-Generation Complex Metal Oxide Nanomaterials Negatively Impact Growth and Development in the Benthic Invertebrate Chironomus riparius upon Settling. *Environmental Science & Technology* **2019,** *53* (7), 3860-3870.
32. Bozich, J.; Hang, M. N.; Hamers, R. J.; Klaper, R. D., Core chemistry influences the toxicity of multicomponent metal oxide nanomaterials, lithium nickel manganese cobalt oxide, and lithium cobalt oxide to Daphnia magna. *Environmental Toxicology and Chemistry* **2017,** *36*.
33. Peréz, C. D. P.; De La Torre Roche, R.; Zuverza-Mena, N.; Ma, C.; Shen, Y.; White, J. C.; Pozza, E. A.; Pozza, A. A. A.; Elmer, W. H., Metalloid and Metal Oxide Nanoparticles Suppress Sudden Death Syndrome of Soybean. *J Agric Food Chem* **2020,** *68* (1), 77-87.
34. Liao, Y. Y.; Strayer-Scherer, A.; White, J. C.; De La Torre-Roche, R.; Ritchie, L.; Colee, J.; Vallad, G. E.; Freeman, J.; Jones, J. B.; Paret, M. L., Particle-size dependent bactericidal activity of magnesium oxide against Xanthomonas perforans and bacterial spot of tomato. *Scientific Reports* **2019,** *9* (1), 18530.
35. Cao, Y.; Ma, C.; Chen, H.; Chen, G.; White, J. C.; Xing, B., Copper stress in flooded soil: Impact on enzyme activities, microbial community composition and diversity in the rhizosphere of Salix integra. *Science of The Total Environment* **2020,** *704*, 135350.
36. Han, X.; Lu, L.; Zheng, Y.; Feng, X.; Li, Z.; Li, J.; Ouyang, M., A review on the key issues of the lithium ion battery degradation among the whole life cycle. *eTransportation* **2019,** *1*, 100005.
37. Wandt, J.; Freiberg, A.; Thomas, R.; Gorlin, Y.; Siebel, A.; Jung, R.; Gasteiger, H. A.; Tromp, M., Transition metal dissolution and deposition in Li-ion batteries investigated by operando X-ray absorption spectroscopy. *Journal of Materials Chemistry A* **2016,** *4* (47), 18300-18305.
38. Rong, X.; Kolpak, A. M., Ab Initio Approach for Prediction of Oxide Surface Structure, Stoichiometry, and Electrocatalytic Activity in Aqueous Solution. *The Journal of Physical Chemistry Letters* **2015,** *6* (9), 1785-1789.
39. Bennett, J. W.; Jones, D.; Huang, X.; Hamers, R. J.; Mason, S. E., Dissolution of Complex Metal Oxides from First-Principles and Thermodynamics: Cation Removal from the (001) Surface of Li(Ni1/3Mn1/3Co1/3)O2. *Environmental Science & Technology* **2018,** *52* (10), 5792-5802.
40. Bennett, J. W.; Jones, D. T.; Hamers, R. J.; Mason, S. E., First-Principles and Thermodynamics Study of Compositionally Tuned Complex Metal Oxides: Cation Release from the (001) Surface of Mn-Rich Lithium Nickel Manganese Cobalt Oxide. *Inorganic Chemistry* **2018,** *57* (21), 13300-13311.
41. Buchman, J. T.; Bennett, E. A.; Wang, C.; Abbaspour Tamijani, A.; Bennett, J. W.; Hudson, B. G.; Green, C. M.; Clement, P. L.; Zhi, B.; Henke, A. H.; *et al.* Nickel enrichment of next-generation NMC nanomaterials alters material stability, causing unexpected dissolution behavior and observed toxicity to S. oneidensis MR-1 and D. magna. *Environmental Science: Nano* **2020,** *7* (2), 571-587.
42. Wagman, D. D.; Evans, W. H.; Parker, V. B.; Schumm, R. H.; Halow, I.; Bailey, S. M.; Churney, K. L.; Nuttall, R. L., Erratum: The NBS tables of chemical thermodynamic properties. Selected values for inorganic and C1 and C2 organic substances in SI units [J. Phys. Chem. Ref. Data 11, Suppl. 2 (1982)]. *Journal of Physical and Chemical Reference Data* **1989,** *18* (4), 1807-1812.

43. Mason, S. E., Forming a Chemically-Guided Basis for Cathode Materials with Reduced Biological Impact using Combined Density Functional Thoery and Thermodynamics Modeling. **2023**.

44. Jain, A.; Ong, S. P.; Hautier, G.; Chen, W.; Richards, W. D.; Dacek, S.; Cholia, S.; Gunter, D.; Skinner, D.; Ceder, G.; Persson, K. A., Commentary: The Materials Project: A materials genome approach to accelerating materials innovation. *APL Materials* **2013,** *1* (1), 011002.

45. Murdock, B. E.; Toghill, K. E.; Tapia-Ruiz, N., A Perspective on the Sustainability of Cathode Materials used in Lithium-Ion Batteries. *Advanced Energy Materials* **2021,** *11* (39), 2102028.

46. Abbaspour-Tamijani, A.; Bennett, J. W.; Jones, D. T.; Cartagena-Gonzalez, N.; Jones, Z. R.; Laudadio, E. D.; Hamers, R. J.; Santana, J. A.; Mason, S. E., DFT and thermodynamics calculations of surface cation release in LiCoO2. *Applied Surface Science* **2020,** *515*, 145865.

47. Bennett, J. W.; Jones, D. T.; Hudson, B. G.; Melendez-Rivera, J.; Hamers, R. J.; Mason, S. E., Emerging investigator series: first-principles and thermodynamics comparison of compositionally-tuned delafossites: cation release from the (001) surface of complex metal oxides. *Environmental Science: Nano* **2020,** *7* (6), 1642-1651.

48. Grimes, R. T.; Bennett, J. W., Surface transformation thermodynamics of alkaline earth carbonates using first-principles calculations. *Surface Science* **2022,** *726*, 122165.

49. Hudson, B. G.; Mason, S. E., Metal Release Mechanism and Electrochemical Properties of Lix(Ni1/3Mn1/3Co1/3)O2. *Applied Sciences* **2022,** *12* (8), 4065.

50. Ma, C.; Borgatta, J.; Hudson, B. G.; Tamijani, A. A.; De La Torre-Roche, R.; Zuverza-Mena, N.; Shen, Y.; Elmer, W.; Xing, B.; Mason, S. E.; *et al.* Advanced material modulation of nutritional and phytohormone status alleviates damage from soybean sudden death syndrome. *Nature Nanotechnology* **2020,** *15* (12), 1033-1042.

51. Sahore, R.; O'Hanlon, D. C.; Tornheim, A.; Lee, C.-W.; Garcia, J. C.; Iddir, H.; Balasubramanian, M.; Bloom, I., Revisiting the Mechanism Behind Transition-Metal Dissolution from Delithiated LiNixMnyCozO2 (NMC) Cathodes. *Journal of The Electrochemical Society* **2020,** *167* (2), 020513.

52. Wachs, S. J.; Behling, C.; Ranninger, J.; Möller, J.; Mayrhofer, K. J. J.; Berkes, B. B., Online Monitoring of Transition-Metal Dissolution from a High-Ni-Content Cathode Material. *ACS Applied Materials & Interfaces* **2021,** *13* (28), 33075-33082.

53. Ruff, Z.; Xu, C.; Grey, C. P., Transition Metal Dissolution and Degradation in NMC811-Graphite Electrochemical Cells. *Journal of The Electrochemical Society* **2021,** *168* (6), 060518.

54. Zheng, H.; Sun, Q.; Liu, G.; Song, X.; Battaglia, V. S., Correlation between dissolution behavior and electrochemical cycling performance for LiNi1/3Co1/3Mn1/3O2-based cells. *Journal of Power Sources* **2012,** *207*, 134-140.

55. Gilbert, J. A.; Shkrob, I. A.; Abraham, D. P., Transition Metal Dissolution, Ion Migration, Electrocatalytic Reduction and Capacity Loss in Lithium-Ion Full Cells. *Journal of The Electrochemical Society* **2017,** *164* (2), A389.

56. Vetter, J.; Novák, P.; Wagner, M. R.; Veit, C.; Möller, K. C.; Besenhard, J. O.; Winter, M.; Wohlfahrt-Mehrens, M.; Vogler, C.; Hammouche, A., Ageing mechanisms in lithium-ion batteries. *Journal of Power Sources* **2005,** *147* (1), 269-281.

57. Gallus, D. R.; Schmitz, R.; Wagner, R.; Hoffmann, B.; Nowak, S.; Cekic-Laskovic, I.; Schmitz, R. W.; Winter, M., The influence of different conducting salts on the metal dissolution and capacity fading of NCM cathode material. *Electrochimica Acta* **2014,** *134*, 393-398.

58. Billy, E.; Joulié, M.; Laucournet, R.; Boulineau, A.; De Vito, E.; Meyer, D., Dissolution Mechanisms of LiNi1/3Mn1/3Co1/3O2 Positive Electrode Material from Lithium-Ion Batteries in Acid Solution. *ACS Applied Materials & Interfaces* **2018,** *10* (19), 16424-16435.

59. Giannozzi, P.; Baroni, S.; Bonini, N.; Calandra, M.; Car, R.; Cavazzoni, C.; Ceresoli, D.; Chiarotti, G. L.; Cococcioni, M.; Dabo, I.; *et al.* QUANTUM ESPRESSO: a modular and open-source software project for quantum simulations of materials. *Journal of Physics: Condensed Matter* **2009,** *21* (39), 395502.

60. Mohanty, D.; Gabrisch, H., Microstructural investigation of LixNi1/3Mn1/3Co1/3O2 (x ≤ 1) and its aged products via magnetic and diffraction study. *Journal of Power Sources* **2012,** *220*, 405-412.

61. Pokhilko, P.; Zgid, D., Evaluation of Neel temperatures from fully self-consistent broken-symmetry GW and high-temperature expansion: application to cubic transition-metal oxides. *arXiv preprint arXiv:2209.14904* **2022**.

62. Taskovic, T.; Eldesoky, A.; Song, W.; Bauer, M.; Dahn, J. R., High Temperature Testing of NMC/Graphite Cells for Rapid Cell Performance Screening and Studies of Electrolyte Degradation. *Journal of The Electrochemical Society* **2022,** *169* (4), 040538.

63. Liu, H.; Liu, H.; Seymour, I. D.; Chernova, N.; Wiaderek, K. M.; Trease, N. M.; Hy, S.; Chen, Y.; An, K.; Zhang, M.; *et al.* Identifying the chemical and structural irreversibility in LiNi0.8Co0.15Al0.05O2 – a model compound for classical layered intercalation. *Journal of Materials Chemistry A* **2018,** *6* (9), 4189-4198.

64. Cahill, L. S.; Yin, S. C.; Samoson, A.; Heinmaa, I.; Nazar, L. F.; Goward, G. R., 6Li NMR Studies of Cation Disorder and Transition Metal Ordering in Li[Ni1/3Mn1/3Co1/3]O2 Using Ultrafast Magic Angle Spinning. *Chemistry of Materials* **2005,** *17* (26), 6560-6566.

65. Kunnikuruvan, S.; Chakraborty, A.; Major, D. T., Monte Carlo- and Simulated-Annealing-Based Funneled Approach for the Prediction of Cation Ordering in Mixed Transition-Metal Oxide Materials. *The Journal of Physical Chemistry C* **2020,** *124* (50), 27366-27377.

66. Bennett, J. W.; Jones, D.; Huang, X.; Hamers, R. J.; Mason, S. E., Dissolution of complex metal oxides from first-principles and thermodynamics: cation removal from the (001) surface of Li(Ni1/3Mn1/3Co1/3)O2. *Environ. Sci. Technol.* **2018,** *52*.

67. Perdew, J. P.; Burke, K.; Ernzerhof, M., Generalized Gradient Approximation Made Simple. *Physical Review Letters* **1996,** *77* (18), 3865-3868.

68. Timrov, I.; Marzari, N.; Cococcioni, M., Hubbard parameters from density-functional perturbation theory. *Physical Review B* **2018,** *98* (8), 085127.

69. Bennett, J. W.; Hudson, B. G.; Metz, I. K.; Liang, D.; Spurgeon, S.; Cui, Q.; Mason, S. E., A systematic determination of hubbard U using the GBRV ultrasoft pseudopotential set. *Computational Materials Science* **2019,** *170*, 109137.

70. Ramadugu, S. K.; Mason, S. E., DFT Study of Antimony(V) Oxyanion Adsorption on α-Al2O3(1$\bar{1}$02). *The Journal of Physical Chemistry C* **2015,** *119* (32), 18149-18159.

71. Huang, X.; Bennett, J. W.; Hang, M. N.; Laudadio, E. D.; Hamers, R. J.; Mason, S. E., Ab Initio Atomistic Thermodynamics Study of the (001) Surface of LiCoO2 in a Water Environment and Implications for Reactivity under Ambient Conditions. *The Journal of Physical Chemistry C* **2017,** *121* (9), 5069-5080.

72. Garrity, K. F.; Bennett, J. W.; Rabe, K. M.; Vanderbilt, D., Pseudopotentials for high-throughput DFT calculations. *Computational Materials Science* **2014,** *81*, 446-452.

73. Monkhorst, H. J.; Pack, J. D., Special points for Brillouin-zone integrations. *Physical Review B* **1976,** *13* (12), 5188-5192.

74. Hudson, B. G.; Mason, S. E., Metal Release Mechanism and Electrochemical Properties of Lix(Ni1/3Mn1/3Co1/3)O2. *Applied Sciences* **2022,** *12* (8).

75. Gagné, O. C.; Hawthorne, F. C., Comprehensive derivation of bond-valence parameters for ion pairs involving oxygen. *Acta Crystallogr B Struct Sci Cryst Eng Mater* **2015,** *71* (Pt 5), 562-78.

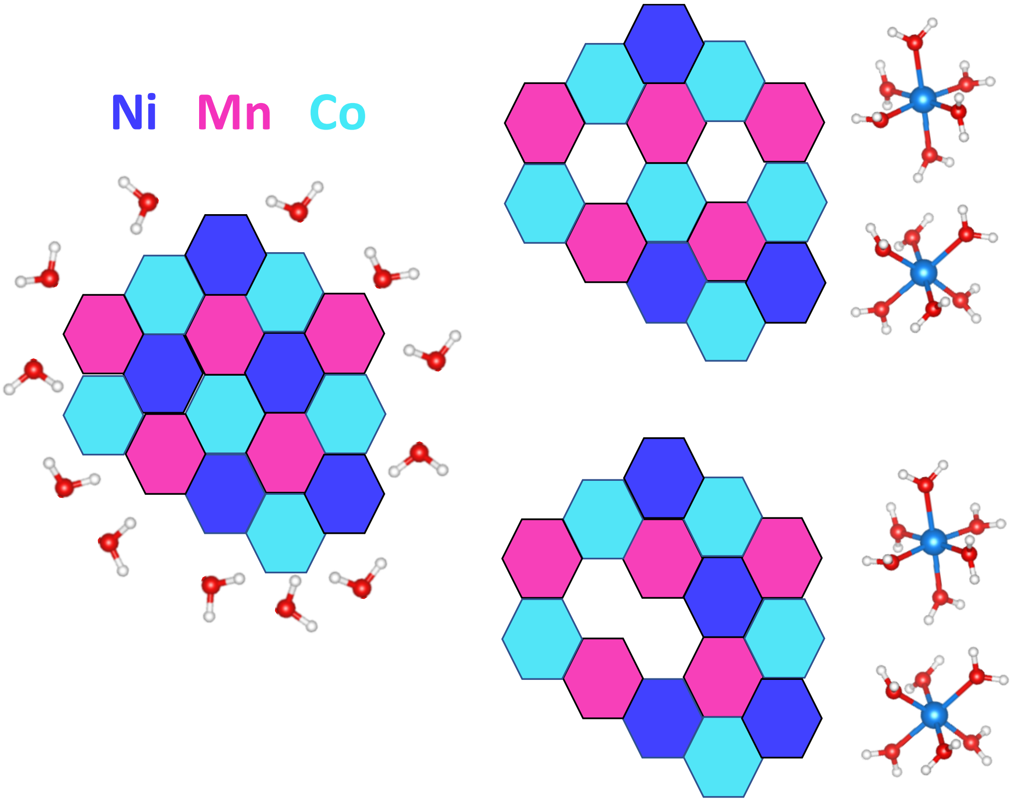

TOC Graphic